

# Particle formation during low-pressure chemical vapor deposition from silane and oxygen: Measurement, modeling, and film properties

T. Kim, S-M. Suh, S. L. Girshick, M. R. Zachariah, and P. H. McMurry<sup>a)</sup>

*Department of Mechanical Engineering, University of Minnesota, Minneapolis, Minnesota 55455*

R. M. Rassel, Z. Shen, and S. A. Campbell

*Department of Electrical and Computer Engineering, University of Minnesota, Minneapolis, Minnesota 55455*

(Received 13 June 2001; accepted 10 December 2001)

Particle generation in thermal chemical vapor deposition (CVD) processes can lead to the formation of contaminant particles that affect film properties and eventually device performance. This article reports on measurements of particle formation during low-pressure CVD of SiO<sub>2</sub> from silane and oxygen. Measurements of aerosol size distributions were made using a particle beam mass spectrometer (PBMS) and were carried out at pressures and temperatures ranging from 0.5 to 2.0 Torr (67–267 Pa) and 200–800 °C, using an O<sub>2</sub>/SiH<sub>4</sub> ratio of 20. We found that within this parameter space, there are three different particle formation regions and a particle-free region. The particle formation regions include an explosion region [200–300 °C,  $P \geq 1.0$  Torr ( $\sim 80$  Pa)], an unsteady region [400–600 °C,  $P \geq 0.8$  Torr ( $\sim 107$  Pa)], and a steady region [700–800 °C,  $P \geq 0.6$  Torr ( $\sim 67$  Pa)]. PBMS size analysis in the steady region shows that the size distributions are bimodal with one mode around 7 nm in diameter and the other around 20 nm, which is in reasonable agreement with transmission electron microscopy measurements. A numerical model was developed to simulate particle nucleation and growth in this system. The model predicts that for a given temperature, there exists a critical pressure above which abundant particle formation occurs and below which particle production is insignificant. The pressures for which particle formation was measured with the PBMS are in good agreement with model predictions, and measured and calculated particle sizes are in reasonable agreement. It is also found that there is a correlation between particle concentration and film surface morphology, dielectric constant, and current–voltage characteristics of the film. © 2002 American Vacuum Society. [DOI: 10.1116/1.1448506]

## I. INTRODUCTION

Contaminant particles formed in semiconductor fabrication processes can lead to a decrease in product yield. A mere 1% decrease in the product yield can cause more than 2% loss in profits.<sup>1</sup> According to the International Technology Roadmap for Semiconductors,<sup>2</sup> the killer particle size, defined as one-half of the gate length, is projected to decrease to 50 nm by the year 2005. Such small particles are typically produced by homogeneous nucleation and growth during fabrication processes. Therefore to meet projected particle contamination control needs, it is essential to understand particle nucleation and growth in the chemically reacting environments, typical of semiconductor processing.

Low-pressure chemical vapor deposition (LPCVD) can be used to produce various thin films, including poly-Si, SiO<sub>2</sub>, and Si<sub>3</sub>N<sub>4</sub>, and is prone to particle contamination problems. We previously reported on an experimental and theoretical study of particle nucleation and growth during the LPCVD of poly-Si films.<sup>3</sup> In extending this work, we chose to focus on particle formation during the LPCVD of SiO<sub>2</sub> from SiH<sub>4</sub> and O<sub>2</sub>, since it has the next simplest chemical reaction mechanism and it is a natural step towards studies of particle formation during plasma-enhanced CVD of SiO<sub>2</sub> films, which we plan for the future. Plasma-enhanced CVD has

largely replaced LPCVD for SiO<sub>2</sub> deposition because it provides higher growth rates and step coverages, and is less prone to particle contamination.

Despite the fact that LPCVD of SiO<sub>2</sub> from SiH<sub>4</sub> and O<sub>2</sub> has been widely used to provide insulation or as a barrier to impurity diffusion,<sup>4</sup> large gaps remain in our understanding of this process: The chemical reaction mechanism of SiO<sub>2</sub> film deposition is not clearly understood and predictive models for particle nucleation and growth are not available. Two primary approaches have been employed to describe the growth of silica thin films. These include those that employ phenomenological models that rely on empirical global gas-phase reactions that are coupled to simple Langmuir–Hinshelwood surface kinetics,<sup>5–14</sup> and those that incorporate a more molecular description of the vapor phase chemistry through the use of elementary reactions.<sup>15–27</sup> Our work is based on the latter approach.

Only a few studies of particle formation during SiO<sub>2</sub> CVD have been reported. Sintani *et al.*<sup>28</sup> measured the size distribution of SiO<sub>2</sub> particles during CVD at atmospheric pressure by observing Mie scattering of He–Ne laser light. They found that the size distribution varies with time, substrate temperature, and reactant concentrations with the predominant particle size in the range of 0.2 to 0.3  $\mu\text{m}$ . They also investigated the effect of these particles on film characteristics.<sup>29</sup> They were unable to find a clear relationship between the presence of gas-borne particles in the reac-

<sup>a)</sup>Electronic mail: mcmurry@me.umn.edu

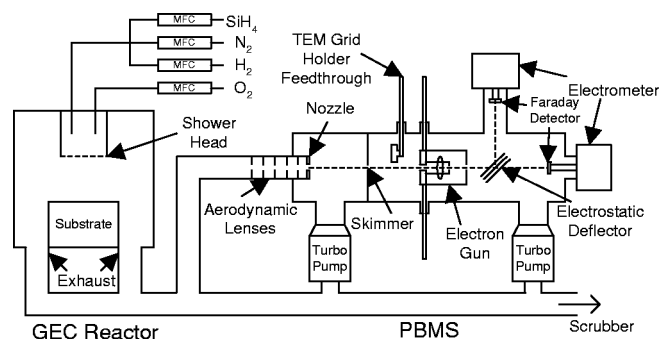


FIG. 1. Schematic of PBMS and CVD reactor for SiO<sub>2</sub> deposition.

tor and the pinhole density or particle contamination of the films. In their experimental study on chemistry and effects on electrical properties of SiO<sub>2</sub> films by LPCVD, Liehr and Cohen<sup>30</sup> varied the reactor temperature and pressure to determine the SiO<sub>2</sub> film growth rate. They identified a particle generation (powder or snow formation) domain, and they found that particles were deposited on the walls of the reactor when gas-borne particles were observed. The experimental conditions used in our study are based on their observations. Finally, Whitby and Hoshino<sup>31</sup> used their low-pressure aerosol sampler<sup>32</sup> to measure the size distribution of particles produced during LPCVD of SiO<sub>2</sub> films. They compared their measurements with predictions of their two-dimensional numerical simulation employing only two gas-phase reactions. They found that particle nucleation rates vary as  $\sim P$ ,<sup>9</sup> where  $P$  is the total pressure, and that below  $\sim 5$  Torr ( $\sim 667$  Pa), particle nucleation rates become negligible. It was also found that 7 cm above the wafer, the particle size distribution is trimodal with modes at 10, 80, and 110 nm. They argued that this is because particle nucleation occurs at three different places: (1) about 2 cm above the center of the wafer, where the temperature is the highest; (2) about 4 cm above the wafer, where the temperatures are lower; and (3) near the edge of the wafer, where the temperature gradients are steep.

In this article we report on measurements of particle formation during LPCVD of SiO<sub>2</sub> from SiH<sub>4</sub> and O<sub>2</sub>, and compare these results to modeling predictions and film properties including surface morphology, dielectric constant, and current-voltage characteristics. Previous studies have provided little qualitative information on the effects of particles on film properties.

## II. EXPERIMENTAL SETUP

### A. Gaseous Electronics Conference cell and particle beam mass spectrometer

Figure 1 shows a schematic of the experimental setup used in this study. It consists of inlet gas mass flow controllers, a Gaseous Electronics Conference (GEC) cell,<sup>33</sup> the exhaust pumping manifold, and the particle beam mass spectrometer (PBMS).<sup>34</sup> The PBMS can sample particles directly from low-pressure environments [ $>100$  mTorr (13 Pa)], detect low particle concentrations ( $>20$  cm<sup>-3</sup>), and measure size distributions of ultrafine particles (0.005–0.5  $\mu$ m) in

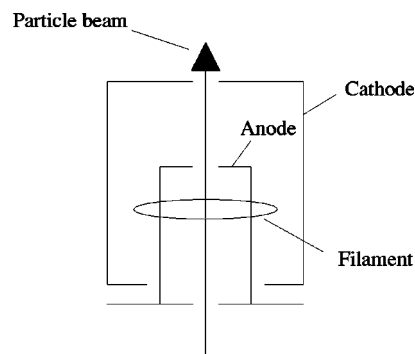


FIG. 2. Schematic of new electron gun.

real time. With this technique, particles sampled from the LPCVD reactor are focused by aerodynamic lenses,<sup>35,36</sup> charged to saturation by electron impact,<sup>37</sup> and classified using an electrostatic energy analyzer.<sup>34</sup> A detailed description of this setup is given by Nijhawan.<sup>3</sup> Because our experiments involved the use of O<sub>2</sub>, the filament used within the electron gun described by Ziemann<sup>34</sup> had a lifetime of only a few hours. Therefore we installed a new electron gun which has a ring-shaped filament made of thoria-coated iridium and has a lifetime of about 3 months. The design of this electron gun, shown schematically in Fig. 2, is adopted from the ionizer design employed in residual gas analyzers made by Stanford Research Systems.<sup>38</sup> The cathode and filament are maintained at  $-190$  V and the anode at  $10$  V so that the electrons have 200 eV of energy.

### B. PBMS data inversion

In an electrostatic field, the voltage needed to obtain enough field strength to deflect incoming particles is proportional to the particle's kinetic energy-to-charge ratio

$$V = mu^2/2Aze, \quad (1)$$

where  $m$ ,  $u$ , and  $z$  are the particle mass, velocity, and charge (in elementary units), respectively.  $A$  is a constant that depends on the deflector angle, and  $e$  is the elementary electron charge. Since the particle mass, velocity, and charge are primarily functions of particle size,<sup>34</sup> this deflection voltage determines a critical particle size,  $D_p(V)$ . All particles below this critical size are deflected by 90°. The deflected particle beam current measured at the off-axis Faraday detector (Fig. 1) is given by

$$I(V) = \int_0^{D_p(V)} \frac{dN}{d \log(D_p)} z(D_p) \eta(D_p) Q e d \log(D_p), \quad (2)$$

where  $dN/d \log(D_p)$  is the particle size distribution function,  $z(D_p)$  is size-dependent particle charge,  $\eta(D_p)$  is transport efficiency from the PBMS inlet to the 90° deflector, and  $Q$  is the volumetric flow rate. When the deflection voltage is sufficiently high to deflect all particles ( $\sim 300$  V), the particle current provides a measure of the total amount of aerosol sampled by the PBMS. We can obtain the particle size distribution function by differentiating Eq. (2):

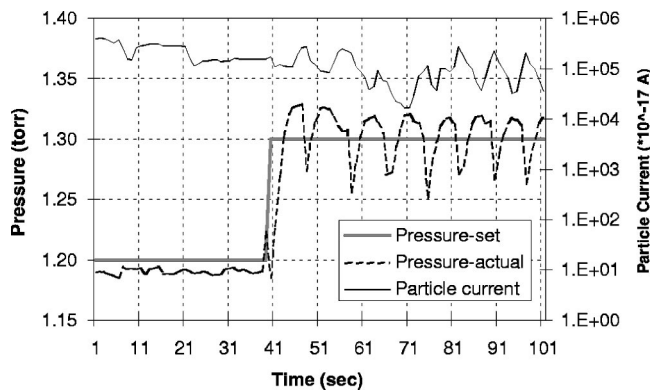


FIG. 3. Particle current measured during SiO<sub>2</sub> deposition at a substrate temperature of 200 °C. Note the appearance of larger pressure fluctuation, when the pressure increased from 1.2 to 1.3 Torr (160–173 Pa).

$$\frac{dN}{d \log(D_p)} = \frac{dI}{dV} \frac{dV}{d \log(D_p)} \frac{1}{z(D_p) \eta(D_p) Qe}. \quad (3)$$

To get the particle size distribution,  $I(V)$  and  $V(D_p)$  are required.  $I(V)$  is obtained by measuring the particle beam current while varying the deflecting voltage and  $V(D_p)$  is obtained from Eq. (1) using the known relationships between particle size and mass, velocity, and charge. These relationships are explained in detail by Ziemann *et al.*<sup>34</sup> The transport efficiency,  $\eta(D_p)$ , is almost unity for particles larger than 20 nm, but decreases rapidly as particle size decreases below 20 nm due to diffusional losses.<sup>35,36</sup>

### C. Experimental conditions

Experiments were performed using an O<sub>2</sub>/SiH<sub>4</sub> ratio of 20, a pressure range from 0.5 to 2.0 Torr (67–267 Pa), and a temperature range from 200 to 800 °C. These conditions were determined from previous studies.<sup>8,28,30,31</sup> Flow rates of reactant gases were controlled with mass flow controllers and the pressure inside the reactor was controlled by the automatic throttle valve installed in the exhaust line. The substrate temperature was maintained by using a proportional integral differential-controlled pyrolytic-graphite heater and the temperature was measured at the center of the substrate using a K-type thermocouple embedded in the substrate holder.

## III. RESULTS AND DISCUSSION

### A. Experimental results

Figure 3 shows the total particle current at a deflection voltage of 300 V measured during the SiO<sub>2</sub> deposition at 200 °C at pressures of 1.2 and 1.3 Torr (160 and 173 Pa). The actual pressure undergoes small fluctuations at 1.2 Torr (160 Pa) and larger fluctuations at 1.3 Torr (173 Pa), but particle currents are one to two orders of magnitude above the PBMS noise,  $\sim 5 \times 10^{-14}$  A. Since the pressure fluctuations can affect the transport efficiency of the particles to the exhaust line, it is difficult to correlate the particle generation and the pressure fluctuation. Optical emission was also observed. These pressure fluctuations start at 1.2 Torr (160 Pa) and

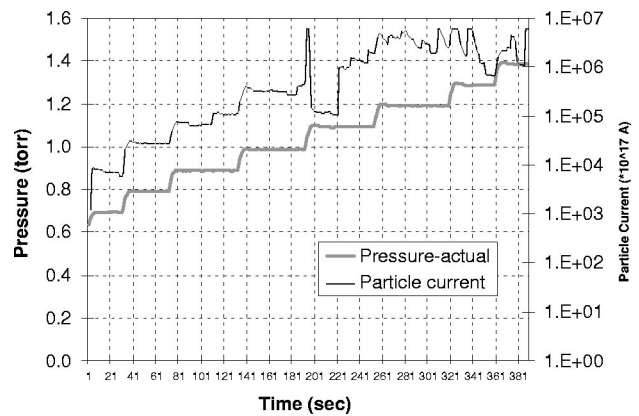


FIG. 4. Particle current measured during SiO<sub>2</sub> deposition at a substrate temperature of 500 °C and pressures changing from 0.7 to 1.4 Torr (93–187 Pa).

become more intense as the pressure is increased to 2.0 Torr (267 Pa). A similar transition from stable to unstable operation was observed at 300 °C as pressure was increased from 0.9 to 1.0 Torr (120–133 Pa). We believe the observed fluctuations are due to explosions within the SiH<sub>4</sub>/O<sub>2</sub> mixture. Previous work by Hartman *et al.*<sup>39</sup> showed that for an O<sub>2</sub>/SiH<sub>4</sub> ratio of 6.1, the lower pressure limit for explosion decreased from 20 Torr (2.6 kPa) at 60 °C to 5 Torr (667 Pa) at 140 °C. Our observed lower pressure limit of explosion of 1.2 Torr (160 Pa) at 200 °C and 1.0 Torr (133 Pa) at 300 °C are consistent with ranges and trends reported by Hartman *et al.* The stability of a mixture for a given temperature and pressure with respect to explosion limits is a competition between chain branching reactions which serve to accelerate the formation of the radical population (H, O, and OH) and chain termination processes which remove radicals. At the pressure and temperature conditions of operations our calculations indicate that we are in a regime where explosions are quite probable and for which radical termination results from diffusional losses to the reactor walls. Indeed, Fig. 3 clearly shows that a small increase in pressure results in explosions (such as have been observed in the H<sub>2</sub>/O<sub>2</sub> system<sup>40</sup>) and is associated with a decreased radical loss to the walls due to the increased pressure.

Figure 4 shows the particle current (deflection voltage set at 300 V) measured during SiO<sub>2</sub> deposition at 500 °C as the pressure was increased from 0.7 to 1.8 Torr (90–240 Pa). Note that the particle current tends to increase as the pressure increases, but fluctuations occur for fixed values of temperature and pressure, and are more pronounced at elevated pressures. Fluctuations are observed at 400, 500, and 600 °C and gradually disappear as the temperature increases. At temperatures above 600 °C, a steady-state particle concentration was achieved as is shown in Fig. 5 for a substrate temperature of 800 °C. The reason for the unsteady particle generation at the intermediate temperatures is not yet known. Also, as the temperature increases, explosions should occur even at lower pressure. The experimental results do not show this trend with increasing temperature and at this point we are at a loss to explain why. However, it can be speculated that at elevated temperatures the showerhead is sufficiently heated by

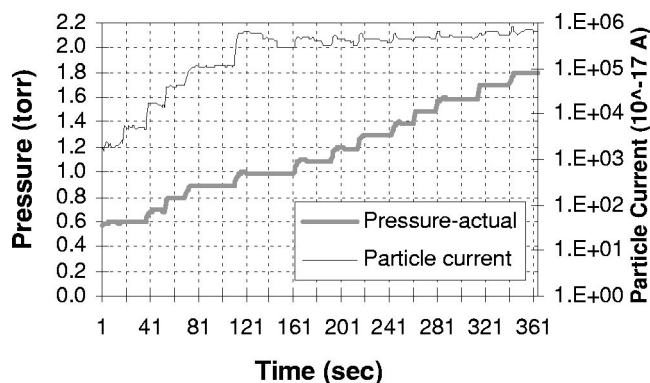


Fig. 5. Particle current measured during SiO<sub>2</sub> deposition at a substrate temperature of 800 °C and pressures changing from 0.6 to 1.8 Torr (80–240 Pa).

radiative effects that the explosion generating chemistry begins at the exit of the showerhead and is therefore quenched due to its proximity to a radical removal surface. It is possible that at the intermediate temperature range below the temperature at which all explosions are quenched, there might exist an unstable reaction domain of unsteady particle formation.

Figure 6 shows the particle current while the temperature was increased from 150 to 800 °C at a pressure of 1.5 Torr (200 Pa), and Fig. 7 shows the particle current while the temperature was decreased from 800 to 150 °C at a pressure of 1.5 Torr (200 Pa). These data provide confirming evidence for the unsteady and steady particle formation domains. Note that the explosion domain is not apparent from particle current data, but was observed from pressure fluctuations. The temperature range for these domains is a bit different when we ramp the substrate temperature up and down. This might be due to the fact that only the substrate temperature is controlled in this experiment. Thus the temperature of the chamber wall and showerhead tends to lag behind. For a given substrate temperature, the average temperature in the reactor will tend to be lower when the substrate temperature is increasing than when it is decreasing.

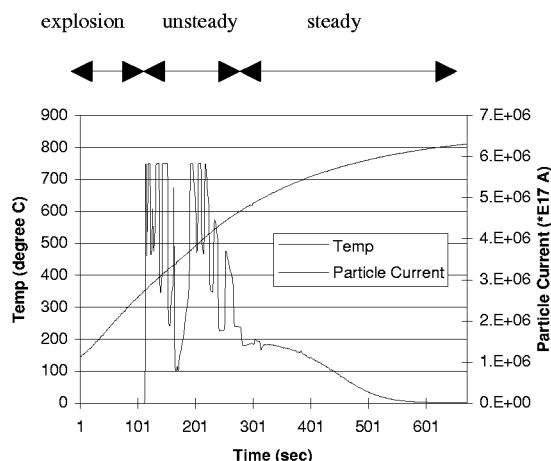


Fig. 6. Particle current measured during SiO<sub>2</sub> deposition at a pressure of 1.5 Torr (200 Pa) and temperatures changing from 150 to 800 °C.

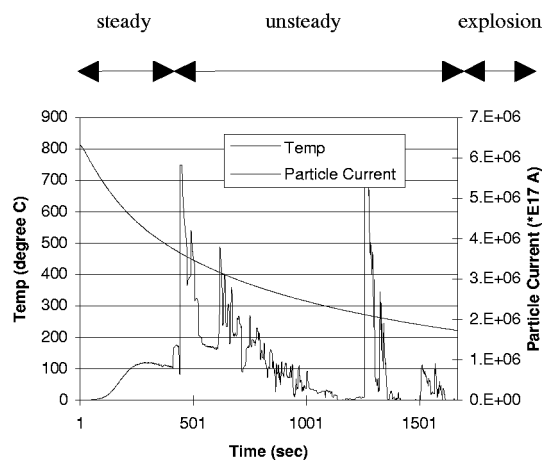


Fig. 7. Particle current measured during SiO<sub>2</sub> deposition at a pressure of 1.5 Torr (200 Pa) and temperatures changing from 800 to 150 °C.

Figure 8 summarizes our observations on the different domains of particle generation during low-pressure CVD of SiO<sub>2</sub> from SiH<sub>4</sub> and O<sub>2</sub> as a function of pressure and temperature: (A) a domain of explosion, chemiluminescence, little particle generation; (B) a domain of unsteady particle generation; (C) a domain of steady particle generation; and (D) a domain of no particle generation. Note that the slope of the line, which separates domain of particle generation and no particle generation, is determined from the least-squares fit of the experimental data shown in Fig. 12.

The PBMS measurements of particle size distribution require steady-state particle generation (domain C). Figure 9 shows the size distribution for particles generated at 800 °C and 1.5 Torr (200 Pa). The distribution is bimodal with modes, ~7 and ~20 nm, which is quite small compared to ~100 nm reported by McMurry *et al.*<sup>41</sup> This discrepancy might be due to the different reactor configuration and SiH<sub>4</sub>/O<sub>2</sub> ratio. McMurry *et al.* used an O<sub>2</sub>/SiH<sub>4</sub> ratio of 1.33 and a horizontal tubular flow reactor (hot-wall type), which allows longer residence times of gases in the reactor and might result in different transport efficiencies of particles to the exhaust line. However, our results are quite compa-

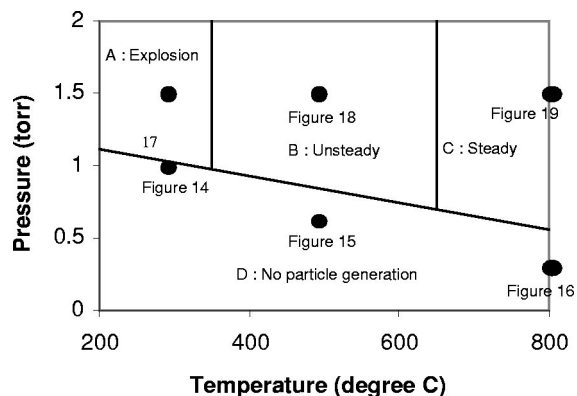


Fig. 8. Pressure–temperature reaction diagram of the CVD of SiO<sub>2</sub> from SiH<sub>4</sub> and O<sub>2</sub>. Black dots indicate the conditions at which the films in Figs. 14–19 were deposited.

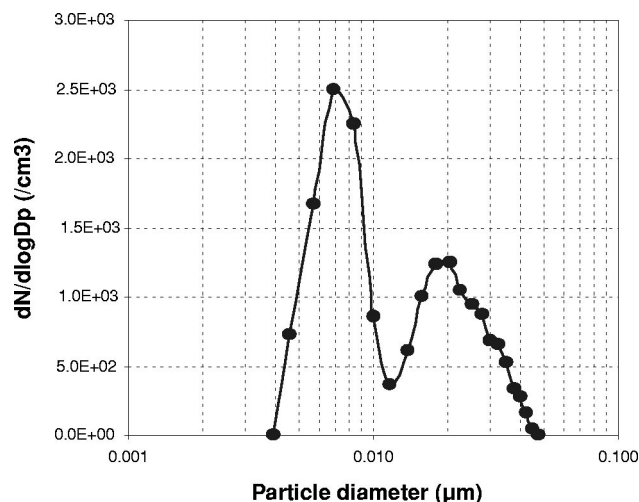


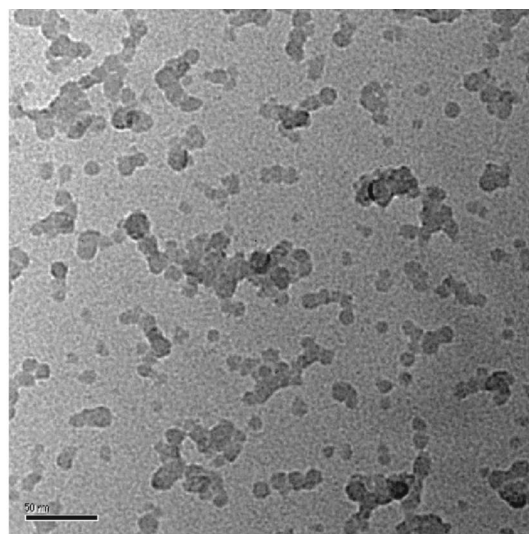
FIG. 9. Particle size distribution during CVD of  $\text{SiO}_2$  from  $\text{SiH}_4$  and  $\text{O}_2$  at 1.5 Torr (200 Pa) and a substrate temperature of 800 °C.

table to those of Whitby and Hoshino,<sup>31</sup> who found that the silicon dioxide particle size distribution is trimodal with the smallest mode around 10 nm. Although they also used a horizontal tubular flow reactor (cold-wall type), they employed the same  $\text{O}_2/\text{SiH}_4$  ratio of 20 (diluted with He) and particles were sampled directly from the chamber to minimize the particle growth.

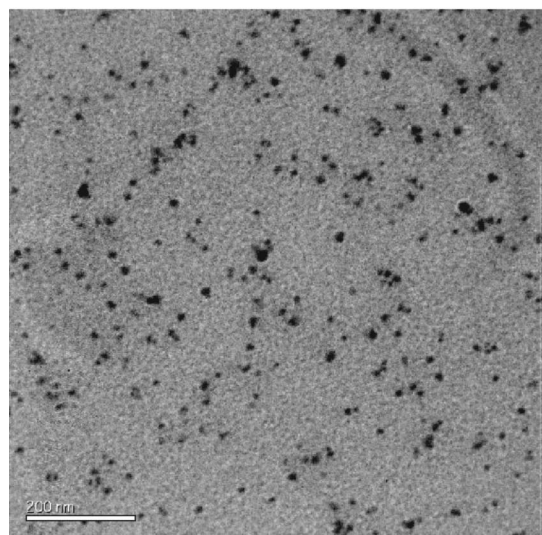
Transmission electron microscopy (TEM) was used to verify the PBMS results. Graphite TEM grids were installed just after the skimmer, at the inlet of the second chamber of the PBMS (Fig. 1). Figure 10(a) shows TEM measurements of  $\text{SiO}_2$  particles generated at 800 °C, 1.5 Torr (200 Pa). The majority of the particles are around 10 nm and there exist some larger particles around 20–25 nm, which agrees well with the PBMS measurements. Some agglomerates are also observed. To test the hypothesis that agglomeration occurred as individual primary particles were deposited on the grid, we collected another sample for which particles were all positively charged by the electron gun before they were collected on the TEM grid. In this case, no agglomerates were observed [Fig. 10(b)]. We believe that electrostatic repulsion prevented the formation of aggregates when this sample was collected. We conclude that particles extracted from the LPCVD reactor consisted of individual particles that were nearly spherical.

## B. Comparisons to modeling results

The model employed in this study is described in detail elsewhere.<sup>42,43</sup> Briefly, four classes of silicon oxide clustering pathways were considered, based on current knowledge of reaction kinetics and cluster properties during low-pressure silane oxidation. The species conservation equations and a moment-type aerosol dynamics model were formulated for a one-dimensional stagnation-point flow geometry which simulates the flow between the showerhead and the substrate in a GEC reference cell reactor. The contributing physical and chemical processes considered in the aerosol dynamics



(a)



(b)

FIG. 10. (a) TEM micrograph of  $\text{SiO}_2$  particles generated at 800 °C, 1.5 Torr. (Scale bar: 50 nm). (b) TEM micrograph of  $\text{SiO}_2$  particles generated at 800 °C, 1.5 Torr. The particles shown in (b) are positively charged to prevent agglomeration while they are deposited. (Scale bar: 200 nm).

model include: homogeneous nucleation; particle growth by surface reactions and coagulation; and particle transport by convection, Brownian diffusion, and thermophoresis. A log-normal particle size distribution was assumed to obtain mathematical expressions for the contributing processes. The chemical clustering model, together with a detailed silane oxidation mechanism and a  $\text{SiO}_2$  film growth mechanism, were coupled to the flow and the aerosol dynamics model.

Figure 11 shows the distribution of particle concentration predicted by our numerical model along the axial direction for reactor pressures ranging from 0.6 to 3 Torr (80–400 Pa) and a substrate temperature of 800 °C. The  $\text{O}_2/\text{SiH}_4$  mixture enters the reactor at a 20:1 ratio. A dramatic increase of particle concentration is predicted as the pressure increases from 0.6 to 0.8 Torr (80–107 Pa), while the particle concen-

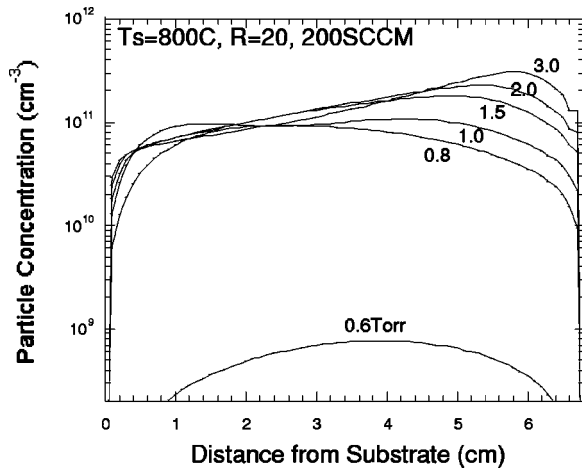


FIG. 11. Calculated particle concentration generated at 800 °C for various processing pressures.

tration becomes relatively insensitive to pressure at higher pressures. Our model assumes that silicon oxide particle formation in this system is largely attributable to the clustering reactions among a few gas species, which include  $\text{SiO}$ ,  $\text{SiO}_2$ ,  $\text{HSiOOH}$ , and  $\text{SiH}_2\text{O}$ . At pressures below 0.8 Torr (107 Pa), diffusion prohibits local accumulation of the clustering species, thereby suppressing particle formation. For pressures above 0.8 Torr (107 Pa), particle generation becomes relatively insensitive to pressure since diffusion becomes less significant at high pressures. We believe this behavior to be universal in nature, based on a recent nondimensionless analysis of particle nucleation in a convection-diffusion environment where we discovered a critical total pressure at which cluster diffusion leads to a dramatic decrease in the particle production rate. These results imply that changes in *total* reactor pressure, even when the precursor concentration is held constant, can lead to significant changes in particle production.

Figure 12 compares the observed onset pressures of particle generation with the model predictions at various sub-

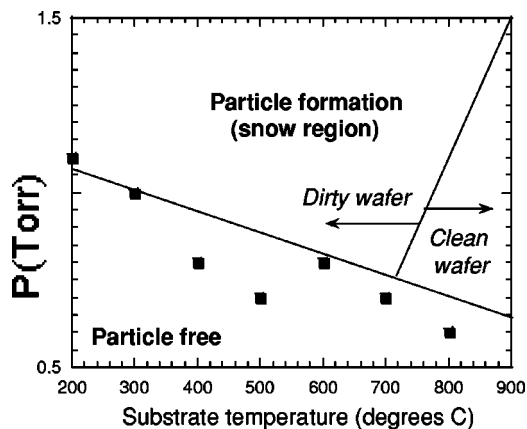


FIG. 12. Comparison between onset of particle generation detected by PBMS and predicted by modeling work. The solid line represents model results and the squares represent measurements. “Dirty wafer” means that the model predicts that particles will deposit on the wafer.

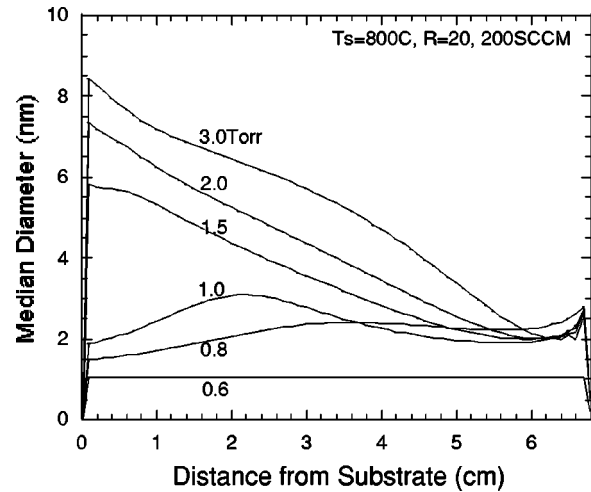


FIG. 13. Calculated particle median diameter generated at 800 °C for various processing pressures.

strate temperatures. The experimental data points represent the minimum pressure at which the PBMS detected particles at a given substrate temperature. Our model also enables us to calculate the particle flux to the wafer. A clean wafer region is predicted at higher substrate temperatures where particles are thermophoretically pushed away from the substrate at lower pressures. As the pressure increases, the substrate-temperature-induced thermophoretic force becomes counterbalanced and finally dominated by the thermophoretic force induced by the exothermicity of the gas-phase chemistry and by the increased particle generation due to the increase in partial pressure of precursor species. Note that this one-dimensional (1D) model does not account for thermophoretic transport to the reactor side walls. As we discuss later, such radial transport may play an important role in determining whether particles are deposited on the wafer or on the reactor wall.

Figure 13 shows the variation in particle median diameter along the axis of the reactor for a temperature of 800 °C and the same range of pressure as in Fig. 11. As mentioned earlier, the model assumes a log-normal size distribution at every axial location. The median particle size is predicted to be less than 10 nm for the range of pressures considered. Since the predicted median sizes of the particles generated at pressures below 1.5 Torr (200 Pa) are smaller than the lower limit of detection of the PBMS, measured and predicted sizes of the particles generated at 1.5 Torr (200 Pa) are compared. As was shown in Fig. 9, bimodal particle size distributions were measured at the exhaust line at 1.5 Torr (200 Pa). The measured size of the first mode, 7 nm, agrees reasonably well with the predicted particle size, ~6 nm, considering that additional growth, not accounted for in the model, might occur as particles travel from the chamber to the exhaust line.

The second mode in Fig. 9 is most likely due to the particle nucleation in a region other than the region between the showerhead and the wafer. Our 1D model does not account for such processes. Whitby and Hoshino<sup>31</sup> argued that the observed trimodal particle size distribution in their study was

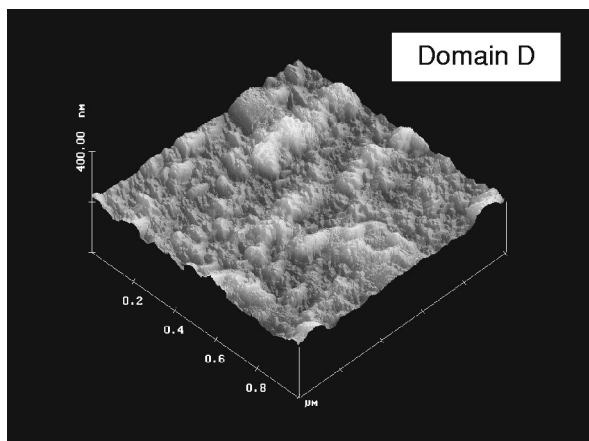


FIG. 14. Atomic force micrograph of SiO<sub>2</sub> film deposited at 1.0 Torr (133 Pa) and 300 °C.

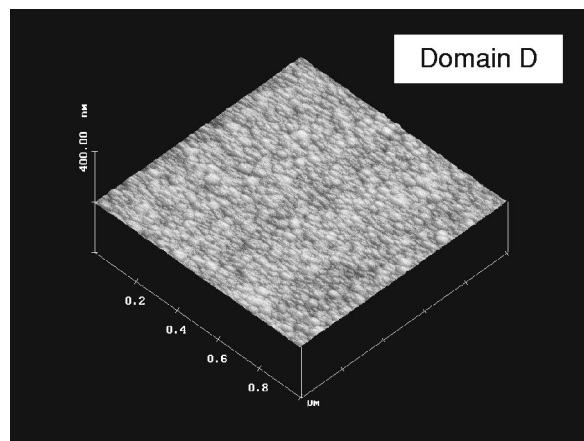


FIG. 16. Atomic force micrograph of SiO<sub>2</sub> film deposited at 0.3 Torr (40 Pa) and 800 °C.

due to the fact that particle nucleation takes place both near the center of the wafer and near its edge, where the temperature gradients are steep. It is possible that similar processes occur in our system and are responsible for the larger mode. However, it is also possible that the larger mode is produced by particles that are formed upstream of the showerhead, where we have observed a residue of particle deposition. SiH<sub>4</sub> and O<sub>2</sub> gases, supplied through two different lines, are mixed before they enter the chamber through the showerhead, which consists of 169 equally spaced concentric holes (305 μm) drilled in a circular disk. The showerhead interior is maintained at a constant temperature using circulating chilled water, but due to radiation from the substrate, its temperature can increase to ~200 °C when the substrate temperature is 800 °C. The elevated temperatures and pressures upstream of the showerhead may promote reactions that lead to nucleation that are not accounted for in our model and which may be responsible for the larger mode.

### C. Comparisons to film property measurements

Atomic force microscopy (AFM) was used to compare the morphology of SiO<sub>2</sub> films deposited in the four regions in Fig. 8. Figures 14–16 show the surface morphology of 1 μm square scans of the SiO<sub>2</sub> film deposited at pressures within the nonparticle generation domain in Fig. 8 and at temperatures of 300, 500, and 800 °C, respectively, for 100 nm thick films. Figures 17–19 show the surface morphology of SiO<sub>2</sub> films deposited at a pressure of 1.5 Torr, which is within the particle generation domain in Fig. 8, and at temperatures of 300, 500, and 800 °C, respectively (domains A, B, and C) with 100–300 nm thick films. The same vertical scale is used on all six figures. Both Figs. 14 and 17 show significant discrete features, which might be associated with imbedded particles, although the density of these features is more pronounced in the sample in which the film was deposited in domain A. Larger mounds and bumps also characterize films deposited in domain A. The topography shown in Fig. 14 has slightly smaller mounds and bumps, however, this processing pressure is very close to the particle generation domain in Fig. 8 for 300 °C. This process pressure was used because

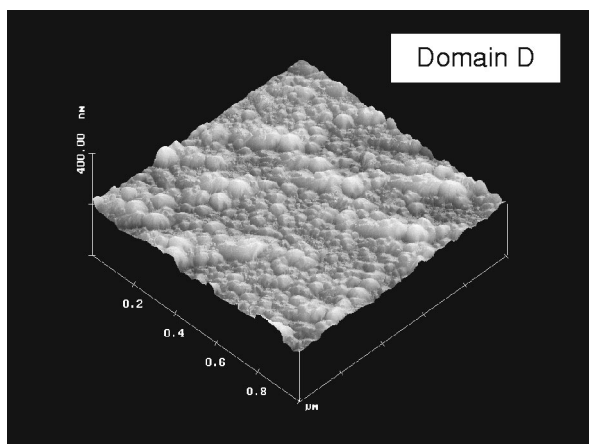


FIG. 15. Atomic force micrograph of SiO<sub>2</sub> film deposited at 0.6 Torr (80 Pa) and 500 °C.

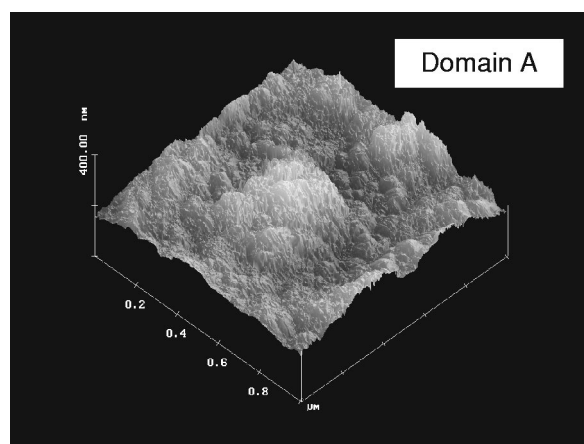


FIG. 17. Atomic force micrograph of SiO<sub>2</sub> film deposited at 1.5 Torr (200 Pa) and 300 °C.

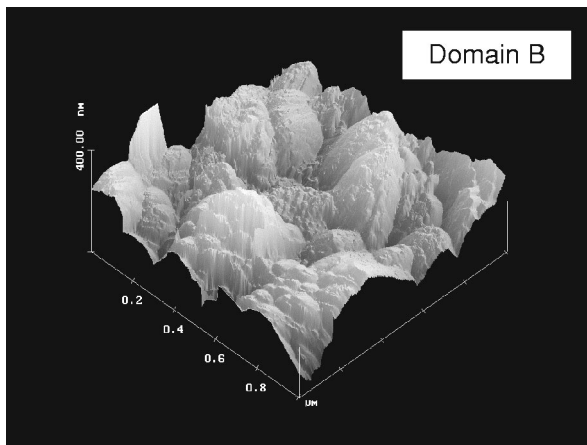


FIG. 18. Atomic force micrograph of  $\text{SiO}_2$  film deposited at 1.5 Torr (200 Pa) and 500 °C.

very little film deposition was observed at 300 °C for pressures below 1 Torr. Comparing Figs. 15 and 18, a dramatic roughening of the surface is observed when processing in the unsteady particle generation domain B. The structures seen in Fig. 17 are still seen in Fig. 18, but the structures are larger with higher densities. Finally, comparison of the high temperature images in Figs. 16 and 19 shows that these films are dramatically different in roughness and features. The film deposited in domain C (Fig. 19) has an extreme topography while the corresponding film in domain D (Fig. 16) is smooth. All of the images obtained from films deposited in the particle generation domain show large and rough features.

To get a more quantitative measure of the surface topography, a  $10 \times 10 \mu\text{m}^2$  region was scanned on the AFM and the rms roughness measured. The results are summarized in Table I. As expected, the film shown in Fig. 18 is much rougher than the film shown in Fig. 15. Less obvious is that the film in Fig. 17, which was deposited in the explosion particle generation domain A, is significantly rougher than the film deposited at the same temperature but at a slightly lower pressure, despite the pressure in that case being near

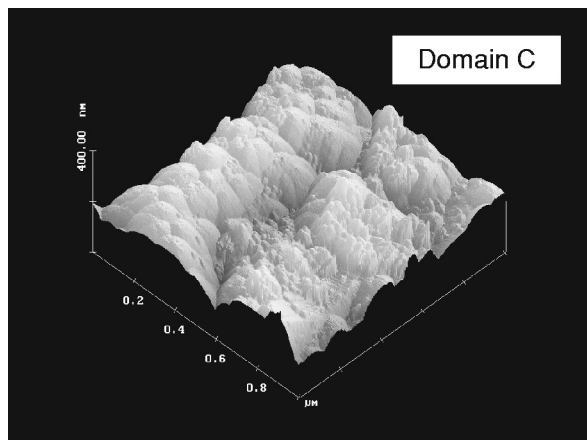


FIG. 19. Atomic force micrograph of  $\text{SiO}_2$  film deposited at 1.5 Torr (200 Pa) and 800 °C.

TABLE I. Results for films deposited in the various particle production regions. Roughness measured by AFM scans over a  $100 \mu\text{m}^2$  area.

Figure No.	Region	Process temperature (°C)	Process pressure (Torr/Pa)	Thickness (nm)	rms roughness (nm)
14		300	1.0/133	158.1	17.1
15	D	500	0.6/80	106.1	11.6
16		800	0.3/40	108.8	1.7
17	A	300	1.5/200	165.4	66.2
18	B	500	1.5/200	283.3	155.6
19	C	800	1.5/200	101.6	76.8

the particle generation domain. Figure 19, which was deposited in the steady state particle production region C, is significantly rougher than the film deposited at the same temperature but within the nonparticle regime. Also, the general reduction of roughening with increasing deposition temperature seen in Figs. 14–16 is not surprising. Since  $\text{SiO}_2$  is amorphous, increasing temperature increases ad molecule mobility without faceting. This increased ad molecule energy should lead to film smoothing by surface diffusion. The roughness measurements seem to confirm the outline of Fig. 8, even though this result is less obvious on the small field scans.

If particles are embedded in the films, they are likely to affect electrical properties of the film as well as film morphology. To measure the electrical properties of the film, capacitors were prepared as shown in Fig. 20. These capacitors consist of a sputter deposited tungsten lower electrode and a sputtered upper aluminum electrode with the CVD  $\text{SiO}_2$  film as an intermediate dielectric layer. They are processed on top of a thick thermal CVD  $\text{SiO}_2$  layer, which is used as a buffer layer to isolate the capacitors from the Si substrate. The metal anode and cathode layers enable us to determine the electrical properties of the sample film. The thickness of the dielectric test film is chosen to be around 1000 Å. The capacitance of these films may be affected by the presence of particles. Knowing the thickness ( $t$ ), area ( $A$ ), and capacitance of the film ( $C$ ), the dielectric constant ( $k$ ) can be calculated by

$$k = Ct/A\epsilon_0, \quad (4)$$

where  $\epsilon_0$  is permittivity constant. The dielectric constant may be different if the chemical composition of the particles is different from that of the film or if the film stoichiometry

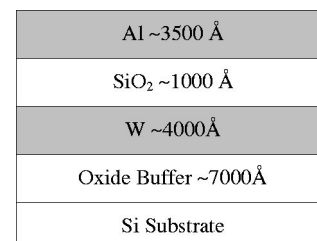


FIG. 20. Schematic of test capacitors.

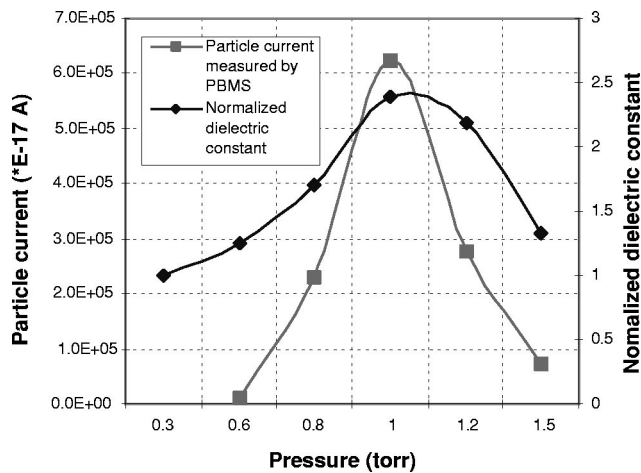


FIG. 21. Comparison between particle current and dielectric constant of the film deposited at a substrate temperature of 800 °C and a pressure range from 0.3 to 1.5 Torr (40–200 Pa).

changes. For example, the dielectric constant of a SiO<sub>2</sub> film ( $k=3.9$ ) containing amorphous silicon particles ( $k=11.7$ ) should be higher than that of a SiO<sub>2</sub> film without such particles. Figure 21 compares dielectric constants of the films deposited at 800 °C and pressures ranging from 0.3 to 1.5 Torr (40–200 Pa) with particle currents measured at the same conditions. The measured dielectric constant is normalized by the value obtained from the film deposited at 0.3 Torr (40 Pa). There appears to be a strong correlation between the dielectric constant of the film and the gas-borne particle concentration. This correlation may be due to embedded particles with a different composition from the film. It is interesting to note that the particle current peaks around 1 Torr and then decreases, although the model (Fig. 13) predicts more particle generation as the pressure increases. The decrease of particle current above 1 Torr (133 Pa) may be due to the decrease in transport efficiency of particles to the exhaust line, caused by the thermophoretic deposition of particles onto the chamber wall.<sup>44</sup> This radial transport is exacerbated by the exothermicity of the O<sub>2</sub>/SiH<sub>4</sub> reaction, which leads to elevated temperatures along the axis. Due to this elevated temperature along the axis, more particles might be transported to the wall than onto the wafer, which would lead to lower dielectric constant of the film. A more detailed understanding of particle transport to the wafer would require a 2D model that would account for the axial and radial transport of particles due to thermophoresis and convection. Note that the 1D model predicts that exothermicity drives particles onto the wafer.

The above measurements suggest that the embedded particles have a dielectric constant that is greater than that of SiO<sub>2</sub>, indicating that they contain less oxygen than SiO<sub>2</sub>. This is consistent with the predictions of our model, which suggests that SiH<sub>2</sub>O and SiO are among four major gas species that are involved in the formation of particles. Although we were unable to quantify the particle composition, we confirmed that some of the embedded particles produce an electron diffraction pattern, indicating that they are crystalline

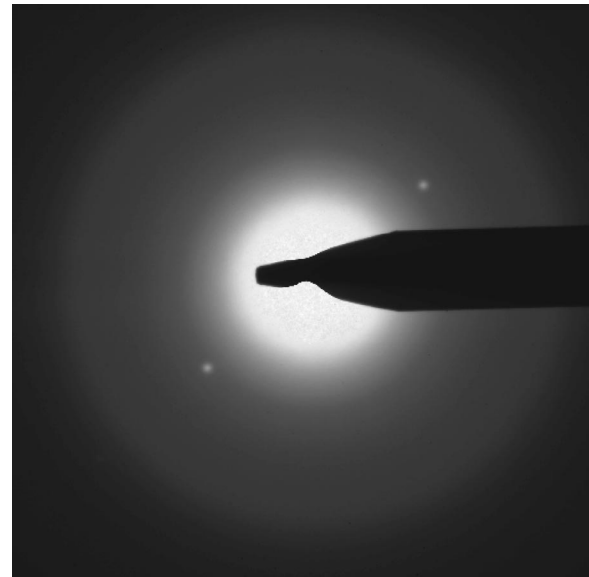


FIG. 22. Diffraction pattern observed from a particle embedded in SiO<sub>2</sub> films deposited at a substrate temperature of 800 °C and a pressure of 1.5 Torr (200 Pa).

(Fig. 22). This supports the argument that the embedded particles are rich in silicon.

The dielectric constant results are supported by measurements of the current–voltage characteristics, the results of which are shown in Fig. 23. As deposition pressures increased from 0.3 to 1.0 Torr (40–133 Pa), leakage currents through the SiO<sub>2</sub> film increased monotonically for a given value of the applied field (shift to the left). However, as deposition pressures increased from 1.0 to 1.5 Torr (133–200 Pa), leakage currents decreased for a given value of the applied field (shift to the right). This effect could conceivably be explained by variations in the film stoichiometry with pressure that mimic the particle concentration. We suspect, however, that the variation of leakage current and the variation in dielectric constant are both related to the variation of Si-rich particles embedded in the film. According to DiMaria and coworkers,<sup>45</sup> electron transport across Si-rich SiO<sub>2</sub> films is controlled primarily by tunneling between the silicon islands. Thus more Si-rich particles in SiO<sub>2</sub> films can cause higher leakage currents. This is explained visually in Fig. 24.

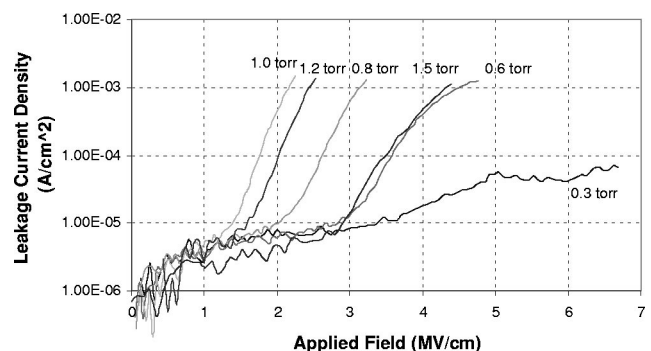


FIG. 23. Current–voltage characteristics of the film deposited at 800 °C for various processing pressures [0.3–1.5 Torr (40–200 Pa)].

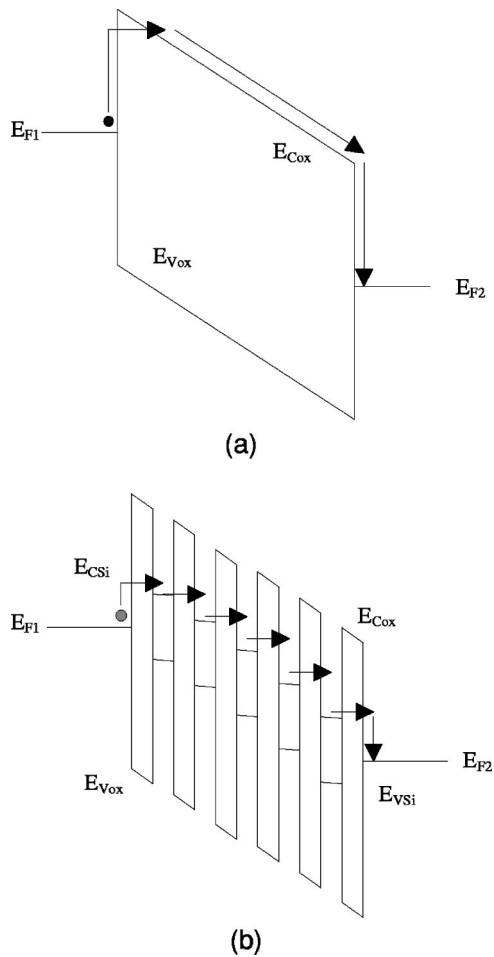


FIG. 24. (a) Standard Fowler–Nordheim injection involves a large ( $\sim 4$  eV) barrier to electron injection into the oxide conduction band and so requires a large bias before substantial current is seen.  $E_{Cox}$ : the bottom of the conduction-band energy for  $\text{SiO}_2$ .  $E_{Vox}$ : the top of the valence-band energy for  $\text{SiO}_2$ .  $E_{F1}$ ,  $E_{F2}$ : Fermi energy. (b) Hopping involves tunneling between silicon islands, which presents much lower barriers to injection.  $E_{Csi}$ : the bottom of the conduction-band energy for Si.  $E_{Vsi}$ : the top of the valence-band energy for Si.

The voltage sweep beyond  $10^{-3}$  A/cm<sup>2</sup> up to capacitor breakdown for the Si-rich particle-embedded capacitors, which is not shown in Fig. 23, exhibits characteristics of charge trapping leading to a screening of the leakage current. Due to the lower electron energy states of Si-rich particles compared to the surrounding  $\text{SiO}_2$  film, electrons can be trapped at Si-rich particles. The electric field generated by these trapped electrons reduces the transport of electrons, which results in a decrease of leakage current. These characteristics will be discussed in a later paper. However, we note that similar charge trapping characteristics with Si nanoparticles have been used to fabricate a nonvolatile silicon nanoparticle memory device.<sup>46</sup>

#### IV. CONCLUSION

This study focused on particle formation during the LPCVD of  $\text{SiO}_2$  films at  $\text{O}_2/\text{SiH}_4$  ratios of 20. Measurements of particle concentrations and size distributions were

compared with the prediction of a numerical model for particle formation and growth. The impact of particle formation on  $\text{SiO}_2$  film properties was also investigated. It was found that there are three different particle formation domains and a particle-free domain for temperatures ranging from 200 to 800 °C and pressures between 0.5 and 2.0 Torr (67–267 Pa). Particle formation domains include an explosion ( $\sim 200$ – $300$  °C), an unsteady ( $\sim 400$ – $600$  °C), and a steady domain ( $\sim 700$ – $800$  °C). In the explosion domain, the pressure was unstable and periodic emission of light was observed. Only a small amount of particle generation is observed during operation in this region. In the unsteady region, the particle concentration fluctuates in a seemingly random manner. Only in the steady region does the generated particle concentration reach steady state. The reason for this phenomenon is not clear yet. Size analysis was performed only in the steady region and a bimodal distribution with modal sizes of  $\sim 7$  and  $\sim 20$  nm was observed at 800 °C and 1.5 Torr (200 Pa). TEM measurements confirm that the particles consist of individual spheres that are smaller than 25 nm, with the majority of particles  $\leq 10$  nm. The model predicts nonparticle and particle generation domains which are in good agreement with experimental observations. Furthermore, the predicted particle size at 800 °C and 1.5 Torr (200 Pa) is comparable to that measured with the PBMS. Film property measurements show that the surface of the films investigated by using AFM is rougher when the films are deposited in a particle-rich domain. The dielectric constant of the films is higher when the films are deposited in a particle-rich domain, which suggests that the composition of the particles embedded in the film is closer to Si than to  $\text{SiO}_2$ . The leakage currents are also higher due to the embedded particles when the films are deposited in the particle-rich domain. These particles can also be a site for charge trapping, which is used to manufacture nonvolatile memory devices.

#### ACKNOWLEDGMENTS

The author thanks Mr. Gyochul Ju from Samsung Electronics for helpful suggestions and comments on experimental work. This research was supported by Semiconductor Research Corporation under Contract No. SRC/97-BJ-442, and by National Science Foundation under Contract No. GOALI. NSF 98-142. The modeling work was supported by the Minnesota Supercomputer Institute.

- <sup>1</sup>J. F. O'Hanlon and H. G. Parks, *J. Vac. Sci. Technol. A* **10**, 1863 (1992).
- <sup>2</sup>*The International Technology Roadmap for Semiconductors* (Semiconductor Industry Association, San Jose, CA, 1999).
- <sup>3</sup>S. Nijhawan, Ph.D. thesis, University of Minnesota, 1999.
- <sup>4</sup>S. A. Campbell, *The Science and Engineering of Microelectronic Fabrication* (Oxford University, New York, 1996).
- <sup>5</sup>B. J. Baliga and S. K. Ghandhi, *J. Appl. Phys.* **44**, 990 (1973).
- <sup>6</sup>J. Middelhoek and A. J. Kinkhamer, presented at the Fifth International Conference on CVD, 1975 (unpublished).
- <sup>7</sup>G. W. Brown, presented at the Fifth International Conference on CVD, 1975 (unpublished).
- <sup>8</sup>M. Shibata and K. Sugawara, *J. Electrochem. Soc.* **122**, 155 (1975).
- <sup>9</sup>M. Maeda and H. Nakamura, *J. Appl. Phys.* **52**, 6651 (1981).
- <sup>10</sup>C. Cobianu and C. Pavelescu, *J. Electrochem. Soc.* **130**, 1888 (1983).
- <sup>11</sup>C. Cobianu and C. Pavelescu, *Thin Solid Films* **102**, 361 (1983).

- <sup>12</sup>P. B. Grabiec and J. Przyluski, *Surf. Coat. Technol.* **25**, 307 (1985).
- <sup>13</sup>P. B. Grabiec and J. Przyluski, *Surf. Coat. Technol.* **25**, 315 (1985).
- <sup>14</sup>P. B. Grabiec and J. Przyluski, *Surf. Coat. Technol.* **27**, 219 (1986).
- <sup>15</sup>H. J. Emeleus and K. Stewart, *J. Chem. Soc.* **1935**, 1182.
- <sup>16</sup>H. J. Emeleus and K. Stewart, *J. Chem. Soc.* **1936**, 677.
- <sup>17</sup>K. Strater, *RCA Rev.* **29**, 618 (1968).
- <sup>18</sup>M. L. Barry, presented at the Second International Conference on Chemical Vapor Deposition, 1970 (unpublished).
- <sup>19</sup>L. L. Vasilyeva, V. N. Drozdov, S. M. Repinsky, and K. K. Svitashv, *Thin Solid Films* **55**, 221 (1978).
- <sup>20</sup>Y. V. Vasiliev, L. L. Vasilieva, V. N. Drozdov, and A. A. Shklyayev, *Thin Solid Films* **76**, 61 (1981).
- <sup>21</sup>E. A. Taft, *J. Electrochem. Soc.* **126**, 1728 (1979).
- <sup>22</sup>P. van de Weijer, B. H. Zwerver, and J. L. G. Suijker, *Chem. Phys. Lett.* **151**, 33 (1988).
- <sup>23</sup>F. B. Ellis, Jr. and J. Houghton, *J. Mater. Res.* **4**, 863 (1989).
- <sup>24</sup>K. Watanabe and H. Komiyama, *J. Electrochem. Soc.* **137**, 1222 (1990).
- <sup>25</sup>T. Kawahara, A. Yuuki, and Y. Matsui, *Jpn. J. Appl. Phys., Part 1* **30**, 431 (1991).
- <sup>26</sup>T. Takahashi, K. Hagiwara, Y. Egashira, and H. Komiyama, *J. Electrochem. Soc.* **143**, 1355 (1996).
- <sup>27</sup>F. Ojeda, A. Castro-Garcia, C. Gomez-Aleixandre, and J. M. Albella, *J. Mater. Res.* **13**, 2308 (1998).
- <sup>28</sup>A. Shintani, K. Suda, M. Suzuki, M. Maki, and K. Takami, *J. Electrochem. Soc.* **124**, 1771 (1977).
- <sup>29</sup>A. Shintani, K. Suda, and M. Maki, *J. Electrochem. Soc.* **127**, 426 (1980).
- <sup>30</sup>M. Liehr and S. A. Cohen, *Appl. Phys. Lett.* **60**, 198 (1992).
- <sup>31</sup>E. Whitby and M. Hoshino, *J. Electrochem. Soc.* **143**, 3397 (1996).
- <sup>32</sup>E. Whitby and M. Hoshino, *Rev. Sci. Instrum.* **66**, 3955 (1995).
- <sup>33</sup>P. J. Hargis, Jr. *et al.*, *Rev. Sci. Instrum.* **65**, 140 (1994).
- <sup>34</sup>P. J. Ziemann, P. Liu, N. P. Rao, D. B. Kittelson, and P. H. McMurry, *J. Aerosol Sci.* **26**, 745 (1995).
- <sup>35</sup>P. Liu, P. J. Ziemann, D. B. Kittelson, and P. H. McMurry, *Aerosol. Sci. Technol.* **22**, 293 (1995).
- <sup>36</sup>P. Liu, P. J. Ziemann, D. B. Kittelson, and P. H. McMurry, *Aerosol. Sci. Technol.* **22**, 314 (1995).
- <sup>37</sup>P. J. Ziemann, P. Liu, D. B. Kittelson, and P. H. McMurry, *J. Phys. Chem.* **99**, 5126 (1995).
- <sup>38</sup>L. Lieszkovszky and A. R. Filippelli, *Vacuum* **7-9**, 2142 (1990).
- <sup>39</sup>J. R. Hartman, J. Famil-Ghiriha, M. A. Ring, and H. E. O'Neal, *Combust. Flame* **68**, 43 (1987).
- <sup>40</sup>S. R. Turns, *An Introduction to Combustion: Concepts and Applications* (McGraw-Hill, New York, 1996).
- <sup>41</sup>P. H. McMurry, S. Nijhawan, N. Rao, P. Ziemann, D. B. Kittelson, and S. Campbell, *J. Vac. Sci. Technol. A* **14**, 582 (1996).
- <sup>42</sup>S.-M. Suh, M. R. Zachariah, and S. L. Girshick, *J. Vac. Sci. Technol. A* **19**, 940 (2001).
- <sup>43</sup>S.-M. Suh, S. Girshick, and M. Zachariah, Second International Symposium on Fundamental Gas-Phase and Surface Chemistry of Vapor-Phase Deposition, 2001 (submitted for proceedings volume).
- <sup>44</sup>S. Nijhawan, P. H. McMurry, and S. A. Campbell, *J. Vac. Sci. Technol. A* **18**, 2198 (2000).
- <sup>45</sup>D. J. DiMaria, D. W. Dong, C. Falcony, T. N. Theis, J. C. Kirtley, J. C. Tsang, and S. D. Brorson, *J. Appl. Phys.* **54**, 5801 (1983).
- <sup>46</sup>T. Maeda, E. Suzuki, I. Sakata, M. Yamanaka, and K. Ishii, *Nanotechnology* **10**, 127 (1999).